

# Programmable refractive functions

Md Sadman Sakib Rahman<sup>1,2,3</sup> mssr@ucla.edu  
Tianyi Gan<sup>1,3</sup> tygan@ucla.edu  
Mona Jarrahi<sup>1,3</sup> mjarrahi@ucla.edu  
Aydogan Ozcan<sup>1,2,3,\*</sup> ozcan@ucla.edu

<sup>1</sup>Electrical and Computer Engineering Department, University of California, Los Angeles, CA, 90095, USA

<sup>2</sup>Bioengineering Department, University of California, Los Angeles, CA, 90095, USA

<sup>3</sup>California NanoSystems Institute (CNSI), University of California, Los Angeles, CA, 90095, USA

\*Corresponding author: [ozcan@ucla.edu](mailto:ozcan@ucla.edu)

## Abstract

Snell's law dictates the phenomenon of light refraction at the interface between two media. Here, we demonstrate, for the first time, arbitrary programming of light refraction through an engineered material where the direction of the output wave can be set independently for different directions of the input wave, covering arbitrarily selected permutations of light refraction between the input and output apertures. Formed by a set of cascaded transmissive layers with optimized phase profiles, this refractive function generator (RFG) spans only a few tens of wavelengths in the axial direction. In addition to monochrome RFG designs, we also report wavelength-multiplexed refractive functions, where a distinct refractive function is implemented at each wavelength through the same engineered material volume, i.e., the permutation of light refraction is switched from one desired function to another function by changing the illumination wavelength. As an experimental proof of concept, we demonstrate negative refractive function at the terahertz part of the spectrum using a 3D-printed material. Arbitrary programming of refractive functions enables new design capabilities for optical materials, devices and systems.

## Introduction

The study of refraction dates back to ancient times when early philosophers like Ptolemy explored the bending of light as it passed through different media. This bending is dictated by the Snell's law, i.e.,  $n_{in} \sin \theta_{in} = n_{out} \sin \theta_{out}$ , where  $n_{in}$  and  $n_{out}$  are the refractive indices of the two media, and  $\theta_{in}$  and  $\theta_{out}$  refer to the angles that the light rays have with respect to the surface normal, while the azimuthal angles of the incident and refracted rays remain the same, i.e.,  $\varphi_{in} = \varphi_{out}$  [1,2]. Advances in nanotechnology have enabled engineering of artificial materials [3–11] with negative effective refractive indices [12–18], causing light to bend in unusual ways and giving rise to phenomena such as anomalous refraction [19,12,20–24] and perfect lensing [25–29]. However, the refractive function that relates the direction of the refracted wave ( $\theta_{out}, \varphi_{out}$ ) to the direction of the incident wave ( $\theta_{in}, \varphi_{in}$ ) is a fixed function determined by the refractive indices of the two media, as described by the Snell's law. This behavior arises from the phase-matching condition [30] of the wavefronts on both sides of an interface. Recognizing this fact allows the tuning of the refractive function along an interface by introducing a phase-gradient, leading to the generalized Snell's law,  $n_{out} \sin \theta_{out} - n_{in} \sin \theta_{in} = \frac{\lambda}{2\pi} \frac{d\psi}{dx}$  where  $\psi$  is the spatial phase distribution at the interface and  $\lambda$  is the wavelength of light [31–35]. Such a phase-gradient can be implemented by using, e.g., gradient metasurfaces, where the properties of the subwavelength inclusions

constituting the meta-atoms vary gradually across a surface [36–43]. While there are reports of tunable refraction realized by adjusting the optical properties of these engineered materials through external stimuli [44–50], at any given state of these materials, the behavior of light refraction for different input directions remains coupled. This prohibits arbitrary programming of the output wave direction independently for each input direction of light; as a result, arbitrary programming of refractive functions could not be achieved with these earlier designs.

Here we demonstrate, for the first time, arbitrary programming of refractive functions through a passive optical device, which we term refractive function generator (RFG); see Fig. 1. In an RFG, the independently optimizable spatial features, i.e., the discrete phase elements, are distributed at a lateral pitch of  $\sim\lambda/2$  over consecutive transmissive layers, axially spanning only  $\sim 15\lambda - 50\lambda$ . Supervised deep learning [51] is used to optimize the collection of these transmissive layers for the implementation of a desired two-dimensional refractive function ( $f$ ), where  $\hat{k}_{out} = f(\hat{k}_{in})$  and  $\hat{k}_{in}, \hat{k}_{out}$  define the propagation directions of the input and output waves, respectively. We report RFG designs that can achieve an arbitrary mapping between the directions of the input and output waves, i.e., for any given direction of input light, the output follows an arbitrarily selected direction for the refracted light, covering any desired permutation function between the input light and the refracted output light. Once the supervised optimization is complete for a given target RFG, the resulting design is fabricated and assembled to form the physical 3D material to perform the desired refractive function between the input and output waves passing through a thin optical volume. In addition to monochrome RFG designs, we also report the use of wavelength multiplexing to simultaneously execute a group of arbitrary refractive functions through the same thin material, each unique function performed at a separate wavelength. In these wavelength-multiplexed RFG designs, switching the illumination wavelength changes the refractive function, covering a set of independent mappings between the directions of the input and output waves. To show the proof of concept of an RFG design, we experimentally demonstrated the programming of negative refractive function ( $\theta_{out} = \theta_{in}, \varphi_{out} = \varphi_{in} + 180^\circ$ ) at the terahertz (THz) part of the spectrum using a 3D-printed device. Without the need for dispersion engineering or deeply sub-wavelength material structures, arbitrary programming of refractive functions opens up new opportunities for the design of advanced optical devices and systems.

## Results

### Design and architecture of an arbitrary refractive function generator (RFG)

The architecture of an RFG is shown in Fig. 1a. A set of  $K$  optimized transmissive surfaces, placed between the input and output apertures, form the core of an RFG. For this work, we only consider phase-only surfaces that modulate the phase of the incident wave. Without loss of generalization, the amplitude modulation is assumed to be negligible, which is a valid assumption here, considering the short axial thickness of an RFG design. The RFG redirects a given input wave, propagating along the direction defined by the unit vector  $\hat{k}_{in}$ , into the output direction  $\hat{k}_{out}$  such that  $\hat{k}_{out} \approx \hat{k}_{target}$ , where  $\hat{k}_{target} = f(\hat{k}_{in})$  and  $f$  is the target/desired refractive function, defining the mapping between the input and output directions. The unit vector  $\hat{k}$  denotes the direction of the wavevector  $\vec{k}$  of a plane wave, i.e.,  $\vec{k} = \frac{2\pi}{\lambda} \hat{k}$ , where  $\lambda$  is the wavelength of light. The unit vector  $\hat{k}$  encapsulates the two angles  $\theta$  and  $\varphi$ , i.e., polar/zenith angle and azimuthal angle [52] in a spherical coordinate system (see Fig. 1a), describing the propagation direction as follows:

$$\hat{k} = \begin{bmatrix} k_x \\ k_y \\ k_z \end{bmatrix} = \begin{bmatrix} \sin \theta \cos \varphi \\ \sin \theta \sin \varphi \\ \cos \theta \end{bmatrix} \quad (1)$$

Since  $k_z^2 = 1 - k_x^2 - k_y^2$ , a more succinct representation of  $\hat{k}$  is the 2D-vector  $(k_x, k_y)$  [53]. Although  $\theta$  and  $\varphi$  can be continuous in principle, the resolution  $\delta_k$  of  $k_x$  and  $k_y$  allowed by a finite aperture of dimension  $D_a$  is also finite [54], i.e.,  $\delta_k \approx \frac{\lambda}{D_a}$ . Therefore, for a given acceptance angle  $\theta_{max}$  (the maximum angle with respect to the  $z$  axis), the set  $\mathbb{K}$  of all  $\hat{k}$  vectors of interest can be written as:  $\mathbb{K} = \left\{ (k_x, k_y): k_x = p \frac{\lambda}{D_a}, k_y = q \frac{\lambda}{D_a}, k_x^2 + k_y^2 < \sin^2 \theta_{max} \right\}$  where  $p$  and  $q$  are integers. The elements of this set are represented by the dots within the circle of radius  $\sin \theta_{max}$  in Fig. 1b, and can be enumerated as  $\{\hat{k}_1, \hat{k}_2, \dots, \hat{k}_{N_m}\}$  where  $N_m = |\mathbb{K}|$  is the number of elements in  $\mathbb{K}$ . An arbitrary refractive function  $f$  can be thought of as a mapping from  $\mathbb{K}$  to  $\mathbb{K}$ , i.e.,  $f: \mathbb{K} \rightarrow \mathbb{K}$ . Each of the dots, defining the set  $\mathbb{K}$ , represents a ‘direction’ that the input or output wave can have.

The mapping of  $\mathbb{K}$  under an arbitrary refractive function  $f$  can be described by a binary  $N_m \times N_m$  matrix  $R$  (such as the ones shown in Fig. 1c), where the 1’s in the matrix define the coupling between  $\hat{k}_{in}$  and  $\hat{k}_{target}$ . In other words,  $R[p, q] = 1$  implies that if  $\hat{k}_{in} = \hat{k}_q$ , then  $\hat{k}_{target} = f(\hat{k}_{in}) = \hat{k}_p$  where  $p, q \in \{1, 2, \dots, N_m\}$ . We show a few examples of such matrices  $R$  and the corresponding mappings of the input directions in Fig. 1c, where each mapping is encoded in the color of the elements of  $\mathbb{K}$ . For example, an identity matrix (first column of Fig. 1c) represents the free-space refractive function ( $\hat{k}_{target} = \hat{k}_{in}$  or  $\theta_{target} = \theta_{in}$ ,  $\varphi_{target} = \varphi_{in}$ ), whereas the flipped identity matrix (second column of Fig. 1c) represents the negative refractive function ( $\theta_{target} = \theta_{in}$ ,  $\varphi_{target} = \varphi_{in} + 180^\circ$ ). A more general form of an arbitrary refractive function can be represented by an arbitrarily selected permutation matrix, which defines an arbitrary mapping between  $\hat{k}_{in}$  and  $\hat{k}_{target}$  (third column of Fig. 1c). As another alternative for  $f$ , we can also envision an arbitrarily filtered and permuted refractive function (fourth column of Fig. 1c), where the input waves traveling in certain arbitrarily chosen directions (the ones corresponding to the columns with all zeros) are filtered out, whereas the waves in the other directions are redirected in a manner following the permutation defined by  $f$  or the corresponding  $R$ .

The design of an RFG follows supervised learning using pairs of input direction  $\hat{k}_{in}$  (equivalently,  $\theta_{in}, \varphi_{in}$ ) and target direction  $\hat{k}_{target}$  (equivalently,  $\theta_{target}, \varphi_{target}$ ), defined based on the desired/target refractive function  $f$  represented by  $R$ . This involves angular spectrum-approach based numerical simulation of wave propagation through a digital model of the RFG (see the Methods section). For a wavefront corresponding to  $\hat{k}_{in}$  at the input aperture, the wavefront leaving the output aperture is numerically simulated; the error between the output wavefront and the wavefront corresponding to  $\hat{k}_{target}$  is backpropagated to update and iteratively optimize the surface phase features using a gradient descent-based algorithm; see the Methods section for details. Unless otherwise stated, we assumed an operating wavelength of  $\lambda = 0.75$  mm for the results shown in the following sections. However, we emphasize that the presented conclusions hold for any wavelength of interest, as long as the dimensions are scaled proportionally to the illumination wavelength,  $\lambda$ .

### Arbitrarily permuted refractive functions

We begin with the design of an arbitrarily permuted refractive function, where the target mapping between the input and output directions is defined by an arbitrarily chosen permutation matrix  $R$  (see Fig.

2a and the 3<sup>rd</sup> column of Fig. 1c). We designed an RFG comprising  $K = 8$  structured surfaces to implement this refractive function, where the axial distance between two consecutive surfaces  $z_{ll}$  was  $6\lambda$ , giving an axial span of  $z_{1K} \approx 50\lambda$  between the first and the last layers. The optimized phase profiles of these surfaces are shown in Fig. 2b. For each input direction  $\hat{k}_{in}$ , the corresponding output angle error is also shown in Fig. 2c. This output angle error  $\varepsilon$  is defined as the angle between  $\hat{k}_{out}$  and  $\hat{k}_{target} = f(\hat{k}_{in})$ . The estimation of the output wave direction  $\hat{k}_{out}$  from the output wavefront is described in the Method section. Figure 2c reveals that the angular errors between the output directions and the target directions are negligible (less than  $0.14^\circ$ ), revealing the success of the RFG in implementing the arbitrarily permuted refractive function, i.e.,  $\hat{k}_{out} \approx \hat{k}_{target} = f(\hat{k}_{in})$ . Supplementary Video 1 also shows the far-field output intensity as the input wave direction is swept, together with the corresponding target patterns that follow  $f$ .

In Fig. 3, we further analyze the errors of the refractive function implementation as the wavelength  $\lambda_{test}$  of input light deviates from the design wavelength  $\lambda_{train}$  that the RFG is trained to operate at. While evaluating the error as a function of  $\lambda_{test}$  we considered two different evaluation metrics: in Fig. 3a, the input and target directions are defined such that  $\sin \theta_{in, \lambda_{test}} = \frac{\lambda_{test}}{\lambda_{train}} \sin \theta_{in, \lambda_{train}}$  and  $\sin \theta_{target, \lambda_{test}} = \frac{\lambda_{test}}{\lambda_{train}} \sin \theta_{target, \lambda_{train}}$  which represents wavefront-preserved testing; as an alternative, in Fig. 3b, we kept the input and target directions at  $\lambda_{test}$  the same as those at  $\lambda_{train}$  which represents angle-preserved testing. The redefinition of directions for the error analysis reported Fig. 3a makes the input and target wavefronts identical to the input and target wavefronts used to train the RFG at  $\lambda_{train}$  even when the illumination wavelength is different, which refers to the wavefront-preserved testing; refer to the Methods section for details. At each test wavelength  $\lambda_{test}$ , the distribution of the angular errors (over  $N_m$  different input directions) is encapsulated with a box-and-whisker diagram in Figs. 3a-b. As expected, the error increases as  $\lambda_{test}$  deviates from  $\lambda_{train}$ . However, the angular errors remain below  $4^\circ$  over a wavelength range of  $\sim 0.99\lambda_{train}$  to  $\sim 1.01\lambda_{train}$  for both the wavefront-preserved testing reported in Fig. 3a and the angle-preserved testing reported in Fig. 3b.

Figure 4 further depicts the dependence of the output errors on the number of structured surfaces  $K$  and the surface-to-surface distance  $z_{ll}$  comprising the RFG structure. For Fig. 4a, we decreased  $K$  from 8 to 3, keeping  $z_{ll} = 6\lambda$ . The output angle errors increased as  $K$  decreased; however, we can see that the errors remain below  $1^\circ$  even when  $K$  is decreased to 4. For Fig. 4b, we set the number of structured surfaces  $K = 4$  and reduced the surface-to-surface distance  $z_{ll}$  from  $6\lambda$  to  $4\lambda$ . On average, the output error increased with a decrease in  $z_{ll}$ . However, even with  $K = 4$  and  $z_{ll} = 4\lambda$ , the output angle errors stay below  $1.6^\circ$ , demonstrating an arbitrarily permuted refractive function with an RFG spanning only  $\sim 15\lambda$  along the axial direction. To clarify, each  $K$  ( $z_{ll}$ ) value in Fig. 4a (4b) represents a separately trained RFG design for the same target refractive function as in Fig. 2a.

An important metric of an RFG design is the output diffraction efficiency (DE), i.e., ratio between the diffracted output power along the target direction and the incident power at the input aperture; see the Methods section. For the RFG reported in Fig. 2, the diffraction efficiencies along the target directions ranged from 0.07% to 0.62%, see the 1<sup>st</sup> row of Fig. 5a. We can tune the diffraction efficiency of an RFG design by properly modifying the training loss function. By using an additional term in the loss function, weighted by  $\eta$  (a training hyperparameter), which penalizes against low diffraction efficiency, we can improve the output diffraction efficiencies of the resulting design with a relatively small sacrifice in the

output error performance. For example, by using  $\eta = 30$ , we can have an RFG design where the maximum output angle error is  $0.87^\circ$ , while the minimum diffraction efficiency increases to 2.75% (see the 3<sup>d</sup> row of Fig 5a). Figure 5b further summarizes the trade-off between the RFG performance and the output diffraction efficiency as a function of  $\eta$ .

### Arbitrarily filtered and permuted refractive functions

Next, we demonstrate the case of an arbitrarily filtered and permuted refractive function. Figure 6a depicts the target refractive function in this case. Here,  $\sim 90\%$  of the input directions are filtered out at the output aperture, whereas the rest are redirected as specified by the non-zero elements of  $R$ ; stated differently,  $R$  in this case refers to an arbitrary permutation matrix with  $\sim 90\%$  of its columns replaced with zeros, corresponding to the filtering of specific directions of input light. To implement this filtered refractive function, we designed an RFG comprising  $K = 8$  surfaces, where the distance between consecutive surfaces  $z_{ll}$  was  $6\lambda$ , yielding an axial span of  $z_{1K} \approx 50\lambda$  between the first and the last surfaces. The optimized phase profiles of these surfaces are shown in Fig. 6e. Figure 6b reveals negligible errors in the output angles for the input directions which are not filtered. At the same time, the diffraction efficiencies along the targeted output directions are  $> 10\%$ ; see Fig. 6c. To evaluate the filtering operation, we also calculated the relative percentage of residual power (i.e., the ratio between the power at the output and the power at the input aperture; see the Methods section) for each one of the filtered-out directions. As shown in Fig. 6d, the relative power transmission is  $< 1\%$  for all the input directions to be filtered, correctly approximating this arbitrarily filtered and permuted refractive function.

### Negative refractive function

We also considered a specific form of refractive function, i.e., the negative refractive function, where  $\theta_{target} = \theta_{in}$  and  $\varphi_{target} = \varphi_{in} + 180^\circ$ ; see the third column of Fig. 1c and Fig. 7. To train for this refractive function,  $\theta_{in}$  and  $\varphi_{in}$  are randomly sampled from the uniform distributions  $\text{Uniform}(0^\circ, \theta_{max} = 60^\circ)$  and  $\text{Uniform}(0^\circ, 360^\circ)$ , respectively. We designed an RFG comprising  $K = 5$  surfaces for implementing the negative refractive function, and the optimized phase profiles are shown in Fig. 7c. For a dense grid of input directions  $\hat{k}_{in}$ , we show the corresponding output angle errors in Fig. 7a and the resulting diffraction efficiencies in Fig. 7b. While the maximum output angle error is  $\sim 2^\circ$ , this relatively large error occurs only when  $\theta_{in}$  is close to  $\theta_{max} = 60^\circ$  because of the limited amount of training data around these angular values at the edges. Figure 7d depicts the ‘operating curve’ of this RFG, which plots the maximum acceptable input angle  $\theta_M$  vs. the maximum acceptable output angle error  $\varepsilon_M$ , such that  $\varepsilon \leq \varepsilon_M$  if  $\theta_{in} \leq \theta_M$ . This plot shows that the RFG can operate at larger input angles if relatively larger errors are tolerated. For example, when  $\theta_{in} \leq 58^\circ$ , the output angle error stays below  $1^\circ$ , as shown in Fig. 7e. Also, Fig. 7b plots the output diffraction efficiency for all the input directions, revealing high diffraction efficiency even without the use of a diffraction efficiency-related term in the training loss function.

### Wavelength multiplexing of arbitrarily permuted refractive functions

Wavelength multiplexing can be used to implement completely different refractive functions, simultaneously executed through the same RFG with a unique refractive function assigned to each wavelength of interest. We demonstrated this wavelength multiplexing capability by designing an RFG that performs three different arbitrarily permuted refractive functions at three different wavelengths, as shown in Fig. 8a, top row. Without loss in generality, we chose the refractive functions such that the corresponding permutation matrices  $R_1$ ,  $R_2$  and  $R_3$  do not have overlapping entries, i.e.,

$\sum_{m,n} R_i[m,n]R_j[m,n] = 0$  if  $i \neq j$ . We chose the wavelengths  $\lambda_1 = 0.70$  mm,  $\lambda_2 = 0.75$  mm and  $\lambda_3 = 0.80$  mm to implement these refractive functions with an RFG comprising  $K = 8$  surfaces. The refractive indices of the assumed RFG material at these wavelengths ( $\lambda_1, \lambda_2, \lambda_3$ ) are  $n_1=1.6512$ ,  $n_2=1.6518$  and  $n_3=1.6524$ , respectively. The optimized thicknesses of the RFG surfaces are shown in Fig. 8b. As depicted in Fig. 8a (second row), the output angle error stays below  $0.5^\circ$  for all the input directions for the three unique refractive functions at the three wavelengths, demonstrating the success of wavelength multiplexing of refractive functions performed simultaneously through the same RFG. Note from the second row of Fig. 8a that the set of input directions for these refractive functions are not identical, since the grid-spacing depends on the wavelength (see Fig. 1b).

It is important to emphasize that this wavelength-multiplexed RFG design does not make use of the dispersion of the transmissive layers for its refractive function implementation accuracy; stated differently, even if we assume that the refractive indices of the assumed RFG material at these wavelengths ( $\lambda_1, \lambda_2, \lambda_3$ ) are equal, i.e.,  $n_1=n_2=n_3=n$ , one could still perform wavelength-multiplexed refractive functions through an RFG design with the same level of accuracy and performance as shown earlier. Supplementary Fig. S2 compares the performance of an alternative design with flat dispersion, where  $n=1.6518$  was selected for all 3 wavelengths, revealing a statistically similar RFG performance as in Fig. 8. These results indicate that the refractive function separation between different illumination wavelengths is based on the wavelength dependence of the free-space propagation kernel, and this unique capability does not need dispersion engineering of specialized materials, which is rather important for practical applications since one can readily work with almost any transmissive substrate that is available at a given desired spectral band.

## Experimental results

We experimentally demonstrated the success of programmable refractive function implementation at THz part of the spectrum with an illumination wavelength of  $\lambda = 0.75$  mm. We designed an RFG comprising  $K = 3$  phase-only surfaces to implement the negative refractive function for  $\theta_{in} \leq \theta_{max} = 30^\circ$ . For this design, the width of the structured surfaces was selected as 80 mm, with a feature size of 0.4 mm, resulting in  $\sim 0.12$  million independently optimizable phase features for the RFG design. The distance between neighboring surfaces was  $\sim 16\lambda$ , giving an axial span of  $z_{1-K} \approx 32\lambda$  for the RFG design.

For resilience against potential misalignments during the experiment, the RFG design was “vaccinated” by applying random lateral shifts ( $\Delta x, \Delta y$ ) to the surfaces during the digital training process. Similarly, the axial distances between the transmissive layers were also vaccinated against imperfections by adding random noise ( $\Delta z$ ) in the optical forward model used during training. These random variables  $\Delta x$ ,  $\Delta y$  and  $\Delta z$  were sampled from uniform distributions, i.e.,  $\text{Uniform}(-0.15\lambda, 0.15\lambda)$ . The optimized phase profiles of the resulting RFG surfaces are shown in Fig. 9a, together with the output angle errors and diffraction efficiencies obtained in numerical simulations.

After the deep learning-based supervised design of the desired RFG, the optimized surfaces were fabricated using a 3D printer and assembled, together with the input and output apertures, to form the physical RFG, as shown in Fig. 9b. This physically assembled RFG was experimentally tested with the system shown in Fig. 9c, which comprises a THz source and a THz scanning detector; see the Methods section for details.

Figure 10 shows the experimentally measured output intensities at an axial distance of  $z = 80$  mm from the output aperture, together with the corresponding simulation results for different input wave

directions defined by  $\theta_{in}$  and  $\varphi_{in}$ . During these experiments, the variation of  $\theta_{in}$  was realized by moving the source horizontally along an arc (see Supplementary Fig. S1b), while the variation of  $\varphi_{in}$  was implemented by in-plane rotation (relative to the source) of the RFG surfaces and the input and output apertures. To compensate for the relative rotation between the RFG and the detector plane, the fields of view (FOVs) corresponding to the experimental measurements were rotated by the same amount (in the opposite direction), as seen in Fig. 10. An additional calibration step to take into account the height of the source relative to the input aperture was also used; see Supplementary Fig. S1a.

Visual assessment of the output intensity patterns in Fig. 10 reveals a very good agreement between the simulated patterns and the measured output patterns. For quantitative analysis, we estimated the direction of the output waves ( $\theta_{out}, \varphi_{out}$ ) from the first moments (center-of-mass) of the diffracted output intensity patterns, which are marked by red dots in Fig. 10; also see Supplementary Fig. S1b. To quantify the mismatch between our simulations and experimental results, the angle between the output directions obtained from each simulation and the corresponding experiment ( $\varepsilon_{sim-exp}$ ) is reported at the bottom of each panel corresponding to a  $(\theta_{in}, \varphi_{in})$  combination. The minimum and maximum values of this angular error,  $\varepsilon_{sim-exp}$ , are  $0.23^\circ$  and  $2.01^\circ$ , which occur at  $(\theta_{in}, \varphi_{in}) = (19.81^\circ, 276.48^\circ)$  and  $(\theta_{in}, \varphi_{in}) = (10.03^\circ, 197.49^\circ)$ , respectively. The mean angular error is  $1.04^\circ$ . These experimental results successfully demonstrate the proof of concept of our refractive function programming capability using the presented framework.

## Methods

### Model of wave propagation through an RFG

The RFG is assumed to comprise  $K$  phase-only transmissive surfaces positioned axially at  $z_1, z_2, \dots, z_K$ , respectively, between the input and the output apertures. The axial positions of the input aperture and the output aperture are denoted by  $z_0$  and  $z_{K+1}$ , respectively. The physical wave propagation between the input and the output aperture is described by successive modulations of the wave by the transmissive surfaces, interleaved by free-space propagation between them. In the following notation,  $w(x, y; z_l^-)$  denotes the wave incident on the diffractive surface at  $z_l$ , whereas  $w(x, y; z_l^+)$  denotes the wave leaving the diffractive surface, after the corresponding phase modulation. The wave propagation through free-space between consecutive surfaces can be described by the Rayleigh-Sommerfeld diffraction integral. For  $l = 1, 2, \dots, K + 1$

$$w(x, y; z_l^-) = \iint w(x', y'; z_{l-1}^+) h_{\text{FSP}}(x - x', y - y'; z_l - z_{l-1}) dx' dy' \quad (2)$$

Here  $w(x, y; z_0^+) = w_{in}(x, y)$  is the input wave and  $h_{\text{FSP}}(x, y; z)$  is the free-space propagation kernel for an axial distance of  $z$ :

$$h_{\text{FSP}}(x, y; z) = \frac{z}{r^2} \left( \frac{1}{2\pi r} + \frac{1}{j\lambda} \right) \exp\left(j \frac{2\pi r}{\lambda}\right) \quad (3)$$

where  $r = \sqrt{x^2 + y^2 + z^2}$ . At the structured surfaces, the incident waves are locally modulated by the corresponding transmittance values that are trainable. For  $l = 1, 2, \dots, K$

$$w(x, y; z_l^+) = t_l(x, y) w(x, y; z_l^-) \quad (4)$$

where  $t_l(x, y)$  is the complex-valued transmittance function of the diffractive surface at  $z_l$ . One can write,



$$t_l(x, y) = a_l(x, y) \exp(j\psi_l(x, y)) \quad (5)$$

where  $a_l(x, y)$  is the local amplitude/absorption and  $\psi_l(x, y)$  is the phase-delay induced by the diffractive surface. For a material with negligible loss,  $a_l(x, y) \approx 1$  whereas the phase delay is related to the local surface thickness  $h_l(x, y)$  as follows:

$$\psi_l(x, y) = \frac{2\pi}{\lambda} (n - 1)h_l(x, y) \quad (6)$$

where  $n$  is the refractive index of the material at the wavelength  $\lambda$ .

In our numerical simulations, free-space propagation of an optical field between successive transmissive surfaces was calculated using the angular spectrum method [55], which is a Fast Fourier transform (FFT)-based implementation of the Rayleigh-Sommerfeld diffraction integral in Eq. (2). The fields/intensities were discretized using  $\delta \approx 0.53\lambda$  along both  $x$  and  $y$ , and sufficiently zero-padded to avoid aliasing [56].

### Experimental setup

A modular amplifier (Virginia Diode Inc. WR9.0 M SGX) with multiplier chain (Virginia Diode Inc. WR4.3x2 WR2.2x2) and a compatible WR2.2 diagonal horn antenna from Virginia Diodes Inc. were used to generate continuous-wave (CW) radiation at 0.4 THz. This was accomplished by amplifying a 10 dBm RF input signal at  $f_{RF1} = 11.1111$  GHz and multiplying it 36 times. To ensure low-noise data acquisition via lock-in detection, the AMC output was modulated at  $f_{MOD} = 1$  kHz. The horn antenna's exit aperture was positioned at ~60 cm from the input aperture of the 3D-printed RFG so that the input THz wavefront was approximately planar. We used a Stratasys Objet30 V2 Pro printer for the 3D fabrication of the resulting RFG design. A single-pixel mixer from Virginia Diodes Inc. detected the diffracted THz radiation at ~80 mm away from the output aperture. The detected signal was down-converted to 1 GHz using a 10 dBm local oscillator signal at  $f_{RF1} = 11.0833$  GHz fed into the mixer. The mixer, mounted on an X-Y positioning stage with two motorized linear stages (Thorlabs NRT100), scanned the output FOV using a  $0.5 \times 0.25$  mm detector with 2 mm intervals. The down-converted signal was amplified by 40 dB using cascaded low-noise amplifiers (Mini-Circuits ZRL-1150-LN+), and unwanted noise was filtered out with a 1 GHz (+/-10 MHz) bandpass filter (KL Electronics 3C40-1000/T10-O/O). After measuring by a low-noise power detector (Mini-Circuits ZX47-60), the output voltage was then measured with a lock-in amplifier (Stanford Research SR830), using the  $f_{MOD} = 1$  kHz modulation signal as a reference, and the amplifier readings were converted to linear scale. While estimating the output wave directions from the experimentally measured intensity patterns (see Supplementary Fig. S1b), only  $5 \times 5$  pixels around the peak intensity was taken into account in calculating the first moment.

### Supplementary Information

Supplementary Information file includes:

- Supplementary Figures S1-S5
- Supplementary Video 1
- Supplementary Methods.



## References

1. M. Born and E. Wolf, *Principles of Optics: Electromagnetic Theory of Propagation, Interference and Diffraction of Light* (Elsevier, 2013).
2. E. Hecht, *Optics* (Pearson Education, Incorporated, 2017).
3. N. Engheta and R. W. Ziolkowski, *Metamaterials: Physics and Engineering Explorations* (John Wiley & Sons, 2006).
4. M. Wegener and S. Linden, "Shaping optical space with metamaterials," *Phys. Today* **63**, 32–36 (2010).
5. A. Poddubny, I. Iorsh, P. Belov, and Y. Kivshar, "Hyperbolic metamaterials," *Nat. Photonics* **7**, 948–957 (2013).
6. S. B. Glybovski, S. A. Tretyakov, P. A. Belov, Y. S. Kivshar, and C. R. Simovski, "Metasurfaces: From microwaves to visible," *Phys. Rep.* **634**, 1–72 (2016).
7. A. Y. Zhu, A. I. Kuznetsov, B. Luk'yanchuk, N. Engheta, and P. Genevet, "Traditional and emerging materials for optical metasurfaces," *Nanophotonics* **6**, 452–471 (2017).
8. S. M. Kamali, E. Arbabi, A. Arbabi, and A. Faraon, "A review of dielectric optical metasurfaces for wavefront control," *Nanophotonics* **7**, 1041–1068 (2018).
9. X. Luo, "Subwavelength Artificial Structures: Opening a New Era for Engineering Optics," *Adv. Mater.* **31**, 1804680 (2019).
10. A. K. Iyer, A. Alù, and A. Epstein, "Metamaterials and Metasurfaces—Historical Context, Recent Advances, and Future Directions," *IEEE Trans. Antennas Propag.* **68**, 1223–1231 (2020).
11. G. Hu, M. Wang, Y. Mazor, C.-W. Qiu, and A. Alù, "Tailoring Light with Layered and Moiré Metasurfaces," *Trends Chem.* **3**, 342–358 (2021).
12. S. Foteinopoulou, E. N. Economou, and C. M. Soukoulis, "Refraction in Media with a Negative Refractive Index," *Phys. Rev. Lett.* **90**, 107402 (2003).
13. J. B. Pendry and D. R. Smith, "Reversing Light With Negative Refraction," *Phys. Today* **57**, 37–43 (2004).
14. T. A. Klar, A. V. Kildishev, V. P. Drachev, and V. M. Shalaev, "Negative-Index Metamaterials: Going Optical," *IEEE J. Sel. Top. Quantum Electron.* **12**, 1106–1115 (2006).
15. E. Ozbay, K. Guven, and K. Aydin, "Metamaterials with negative permeability and negative refractive index: experiments and simulations," *J. Opt. Pure Appl. Opt.* **9**, S301 (2007).
16. H. J. Lezec, J. A. Dionne, and H. A. Atwater, "Negative Refraction at Visible Frequencies," *Science* **316**, 430–432 (2007).
17. C. M. Soukoulis, S. Linden, and M. Wegener, "Negative Refractive Index at Optical Wavelengths," *Science* **315**, 47–49 (2007).
18. V. Bruno, C. DeVault, S. Vezzoli, Z. Kudyshev, T. Huq, S. Mignuzzi, A. Jacassi, S. Saha, Y. D. Shah, S. A. Maier, D. R. S. Cumming, A. Boltasseva, M. Ferrera, M. Clerici, D. Faccio, R. Sapienza, and V. M. Shalaev, "Negative Refraction in Time-Varying Strongly Coupled Plasmonic-Antenna--Epsilon-Near-Zero Systems," *Phys. Rev. Lett.* **124**, 043902 (2020).
19. C. Luo, S. G. Johnson, J. D. Joannopoulos, and J. B. Pendry, "All-angle negative refraction without negative effective index," *Phys. Rev. B* **65**, 201104 (2002).
20. E. Cubukcu, K. Aydin, E. Ozbay, S. Foteinopoulou, and C. M. Soukoulis, "Negative refraction by photonic crystals," *Nature* **423**, 604–605 (2003).
21. A. Belardini, F. Pannone, G. Leahu, M. C. Larciprete, M. Centini, C. Sibilia, C. Martella, M. Giordano, D. Chiappe, and F. Buatier de Mongeot, "Evidence of anomalous refraction of self-assembled curved gold nanowires," *Appl. Phys. Lett.* **100**, 251109 (2012).

22. N. K. Grady, J. E. Heyes, D. R. Chowdhury, Y. Zeng, M. T. Reiten, A. K. Azad, A. J. Taylor, D. A. R. Dalvit, and H.-T. Chen, "Terahertz Metamaterials for Linear Polarization Conversion and Anomalous Refraction," *Science* **340**, 1304–1307 (2013).
23. D. Sell, J. Yang, E. W. Wang, T. Phan, S. Doshay, and J. A. Fan, "Ultra-High-Efficiency Anomalous Refraction with Dielectric Metasurfaces," *ACS Photonics* **5**, 2402–2407 (2018).
24. N. L. Tsitsas and C. Valagiannopoulos, "Anomalous refraction into free space with all-dielectric binary metagratings," *Phys. Rev. Res.* **2**, 033526 (2020).
25. J. B. Pendry, "Negative Refraction Makes a Perfect Lens," *Phys. Rev. Lett.* **85**, 3966–3969 (2000).
26. J. B. Pendry and S. A. Ramakrishna, "Focusing light using negative refraction," *J. Phys. Condens. Matter* **15**, 6345 (2003).
27. P. V. Parimi, W. T. Lu, P. Vodo, and S. Sridhar, "Imaging by flat lens using negative refraction," *Nature* **426**, 404–404 (2003).
28. E. Ozbay and K. Aydin, "Negative refraction and imaging beyond the diffraction limit by a two-dimensional left-handed metamaterial," *Photonics Nanostructures - Fundam. Appl.* **6**, 108–115 (2008).
29. M. Khorasaninejad, W. T. Chen, R. C. Devlin, J. Oh, A. Y. Zhu, and F. Capasso, "Metalenses at visible wavelengths: Diffraction-limited focusing and subwavelength resolution imaging," *Science* **352**, 1190–1194 (2016).
30. B. E. A. Saleh and M. C. Teich, *Fundamentals of Photonics* (John Wiley & Sons, 2019).
31. N. Yu, P. Genevet, M. A. Kats, F. Aieta, J.-P. Tetienne, F. Capasso, and Z. Gaburro, "Light Propagation with Phase Discontinuities: Generalized Laws of Reflection and Refraction," *Science* **334**, 333–337 (2011).
32. F. Aieta, A. Kabiri, P. Genevet, N. Yu, M. A. Kats, Z. Gaburro, and F. Capasso, "Reflection and refraction of light from metasurfaces with phase discontinuities," *J. Nanophotonics* **6**, 063532 (2012).
33. X. Ni, N. K. Emani, A. V. Kildishev, A. Boltasseva, and V. M. Shalaev, "Broadband Light Bending with Plasmonic Nanoantennas," *Science* **335**, 427–427 (2012).
34. L. Zheng and Y. Zhao, "Generalized Snell's Law and Its Verification by Metasurface," in *Innovative Mobile and Internet Services in Ubiquitous Computing*, L. Barolli, A. Poniszewska-Maranda, and H. Park, eds. (Springer International Publishing, 2021), pp. 364–372.
35. M. Schake, "Examining and explaining the "generalized laws of reflection and refraction" at metasurface gratings," *JOSA A* **39**, 1352–1359 (2022).
36. S. Sun, K.-Y. Yang, C.-M. Wang, T.-K. Juan, W. T. Chen, C. Y. Liao, Q. He, S. Xiao, W.-T. Kung, G.-Y. Guo, L. Zhou, and D. P. Tsai, "High-Efficiency Broadband Anomalous Reflection by Gradient Metasurfaces," *Nano Lett.* **12**, 6223–6229 (2012).
37. A. Pors, M. G. Nielsen, R. L. Eriksen, and S. I. Bozhevolnyi, "Broadband Focusing Flat Mirrors Based on Plasmonic Gradient Metasurfaces," *Nano Lett.* **13**, 829–834 (2013).
38. D. Lin, P. Fan, E. Hasman, and M. L. Brongersma, "Dielectric gradient metasurface optical elements," *Science* **345**, 298–302 (2014).
39. N. M. Estakhri and A. Alù, "Recent progress in gradient metasurfaces," *JOSA B* **33**, A21–A30 (2016).
40. N. Mohammadi Estakhri and A. Alù, "Wave-front Transformation with Gradient Metasurfaces," *Phys. Rev. X* **6**, 041008 (2016).
41. F. Ding, A. Pors, and S. I. Bozhevolnyi, "Gradient metasurfaces: a review of fundamentals and applications," *Rep. Prog. Phys.* **81**, 026401 (2017).
42. Z. Li, M.-H. Kim, C. Wang, Z. Han, S. Shrestha, A. C. Overvig, M. Lu, A. Stein, A. M. Agarwal, M. Lončar, and N. Yu, "Controlling propagation and coupling of waveguide modes using phase-gradient metasurfaces," *Nat. Nanotechnol.* **12**, 675–683 (2017).

43. H. Kazemi, M. Albooyeh, and F. Capolino, "Simultaneous Perfect Bending and Polarization Rotation of Electromagnetic Wavefront Using Chiral Gradient Metasurfaces," *Phys. Rev. Appl.* **13**, 024078 (2020).
44. M. Peccianti, A. Dyadyusha, M. Kaczmarek, and G. Assanto, "Tunable refraction and reflection of self-confined light beams," *Nat. Phys.* **2**, 737–742 (2006).
45. J. Kästel, M. Fleischhauer, S. F. Yelin, and R. L. Walsworth, "Tunable Negative Refraction without Absorption via Electromagnetically Induced Chirality," *Phys. Rev. Lett.* **99**, 073602 (2007).
46. H. Cheng, S. Chen, P. Yu, W. Liu, Z. Li, J. Li, B. Xie, and J. Tian, "Dynamically Tunable Broadband Infrared Anomalous Refraction Based on Graphene Metasurfaces," *Adv. Opt. Mater.* **3**, 1744–1749 (2015).
47. J. Y. Kim, H. Kim, B. H. Kim, T. Chang, J. Lim, H. M. Jin, J. H. Mun, Y. J. Choi, K. Chung, J. Shin, S. Fan, and S. O. Kim, "Highly tunable refractive index visible-light metasurface from block copolymer self-assembly," *Nat. Commun.* **7**, 12911 (2016).
48. H. Hu, N. Chen, H. Teng, R. Yu, M. Xue, K. Chen, Y. Xiao, Y. Qu, D. Hu, J. Chen, Z. Sun, P. Li, F. J. G. de Abajo, and Q. Dai, "Gate-tunable negative refraction of mid-infrared polaritons," *Science* **379**, 558–561 (2023).
49. Z. Tao, X. Wan, B. C. Pan, and T. J. Cui, "Reconfigurable conversions of reflection, transmission, and polarization states using active metasurface," *Appl. Phys. Lett.* **110**, 121901 (2017).
50. A. Fallah, M. Camacho, and N. Engheta, "Electron-Sheet Metasurfaces for Reconfigurable Beam Patterns," *IEEE Antennas Wirel. Propag. Lett.* **21**, 2201–2205 (2022).
51. Y. LeCun, Y. Bengio, and G. Hinton, "Deep learning," *Nature* **521**, 436–444 (2015).
52. G. A. Korn and T. M. Korn, *Mathematical Handbook for Scientists and Engineers: Definitions, Theorems, and Formulas for Reference and Review* (Courier Corporation, 2013).
53. L. Novotny and B. Hecht, *Principles of Nano-Optics*, 2nd ed. (Cambridge University Press, 2012).
54. A. V. Oppenheim, A. S. Willsky, and S. H. Nawab, *Signals & Systems* (Prentice-Hall International, 1997).
55. J. W. Goodman, *Introduction to Fourier Optics*, McGraw-Hill Physical and Quantum Electronics Series (W. H. Freeman, 2005).
56. T. Kozacki and K. Falaggis, "Angular spectrum-based wave-propagation method with compact space bandwidth for large propagation distances," *Opt. Lett.* **40**, 3420–3423 (2015).
57. D. P. Kingma and J. Ba, "Adam: A Method for Stochastic Optimization," (2017).
58. M. Abadi, P. Barham, J. Chen, Z. Chen, A. Davis, J. Dean, M. Devin, S. Ghemawat, G. Irving, M. Isard, M. Kudlur, J. Levenberg, R. Monga, S. Moore, D. G. Murray, B. Steiner, P. Tucker, V. Vasudevan, P. Warden, M. Wicke, Y. Yu, and X. Zheng, "TensorFlow: a system for large-scale machine learning," in *Proceedings of the 12th USENIX Conference on Operating Systems Design and Implementation, OSDI'16* (USENIX Association, 2016), pp. 265–283.

# Figures

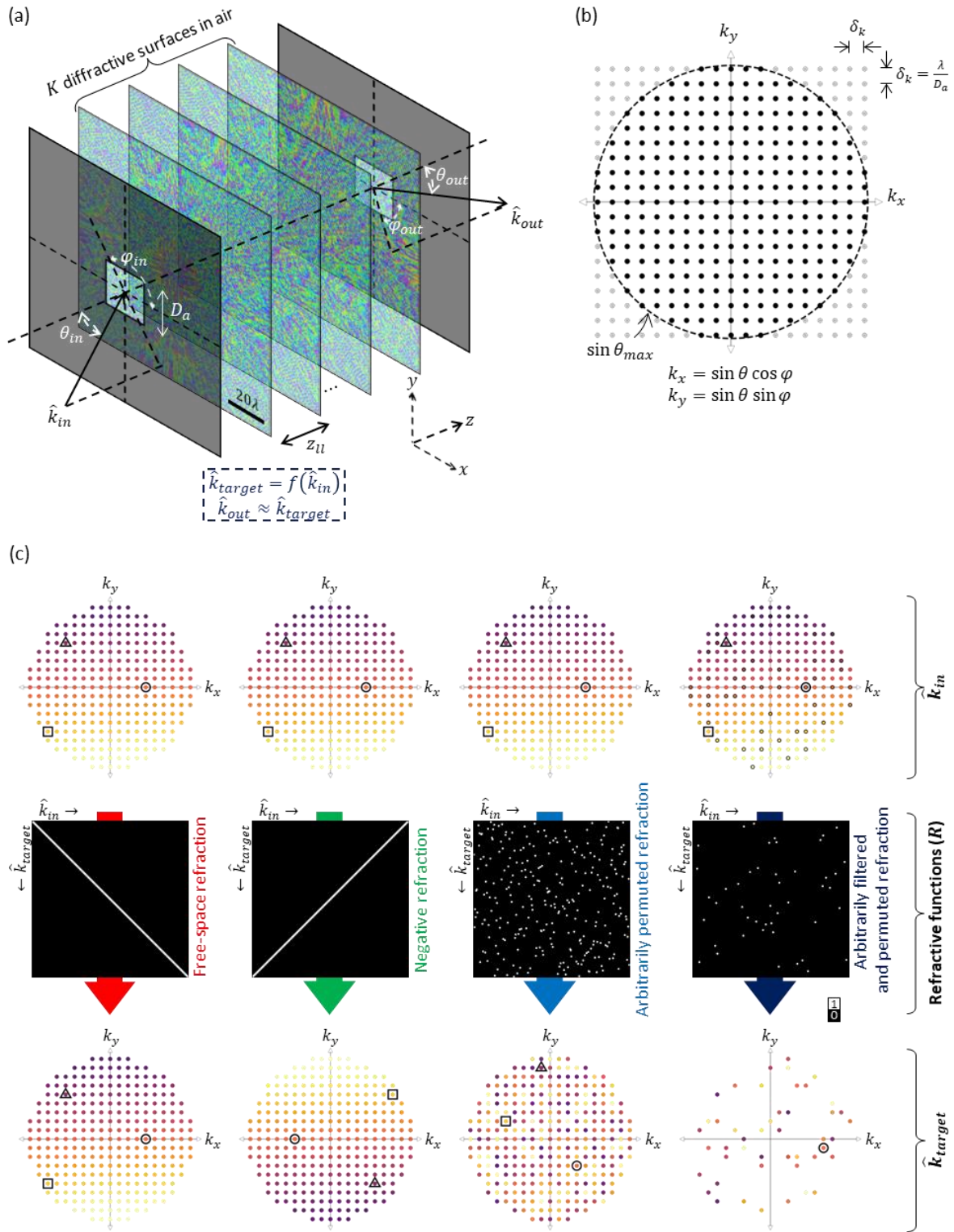


**Fig. 1:** Programming refractive functions. (a) An RFG comprising  $K$  transmissive surfaces in air with an axial separation of  $z_{1l}$  between the successive surfaces (e.g.,  $z_{1l} \sim 6\lambda$ ). The RFG refracts an input wave along

the direction  $\hat{k}_{in}$  into the direction  $\hat{k}_{out}$ , where  $\hat{k}_{out} \approx \hat{k}_{target} = f(\hat{k}_{in})$  and  $f$  is the target refractive function of interest. (b) The set of all  $\hat{k}$  vectors of interest for a given maximum angle  $\theta_{max}$  and a finite aperture width of  $D_a$ , represented by the dots. (c) The mapping of the  $\hat{k}$  vectors under different refractive functions  $f$  represented by the binary matrices  $R$ . The mapping is encoded in the color of the dots. For visual aid, the mappings of three  $\hat{k}$  vectors are also highlighted with a triangle, a circle, and a square to guide the eye.

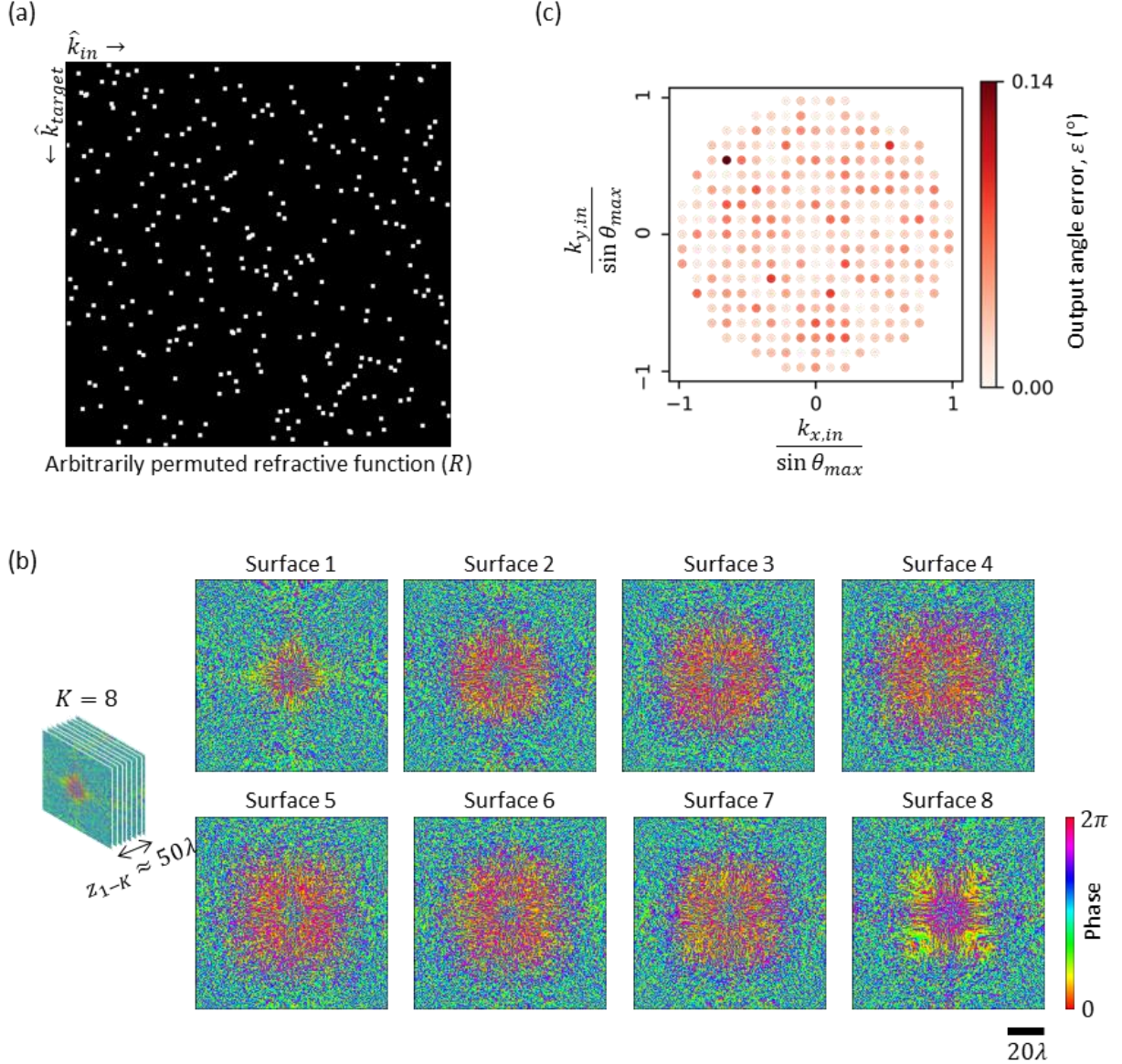


**Fig. 2:** Arbitrarily permuted refractive function implementation with a  $K = 8$  RFG design. (a) The matrix  $R$  representing the arbitrarily permuted refractive function, the same as the one depicted in Fig. 1c, 3<sup>rd</sup> column. (b) The optimized phase profiles of the RFG surfaces. Here  $z_{ll} \approx 6\lambda$ , giving a total axial thickness of  $z_{1-K} \approx 50\lambda$  between the first and the last surfaces. (c) The error in output angles for all the input directions.

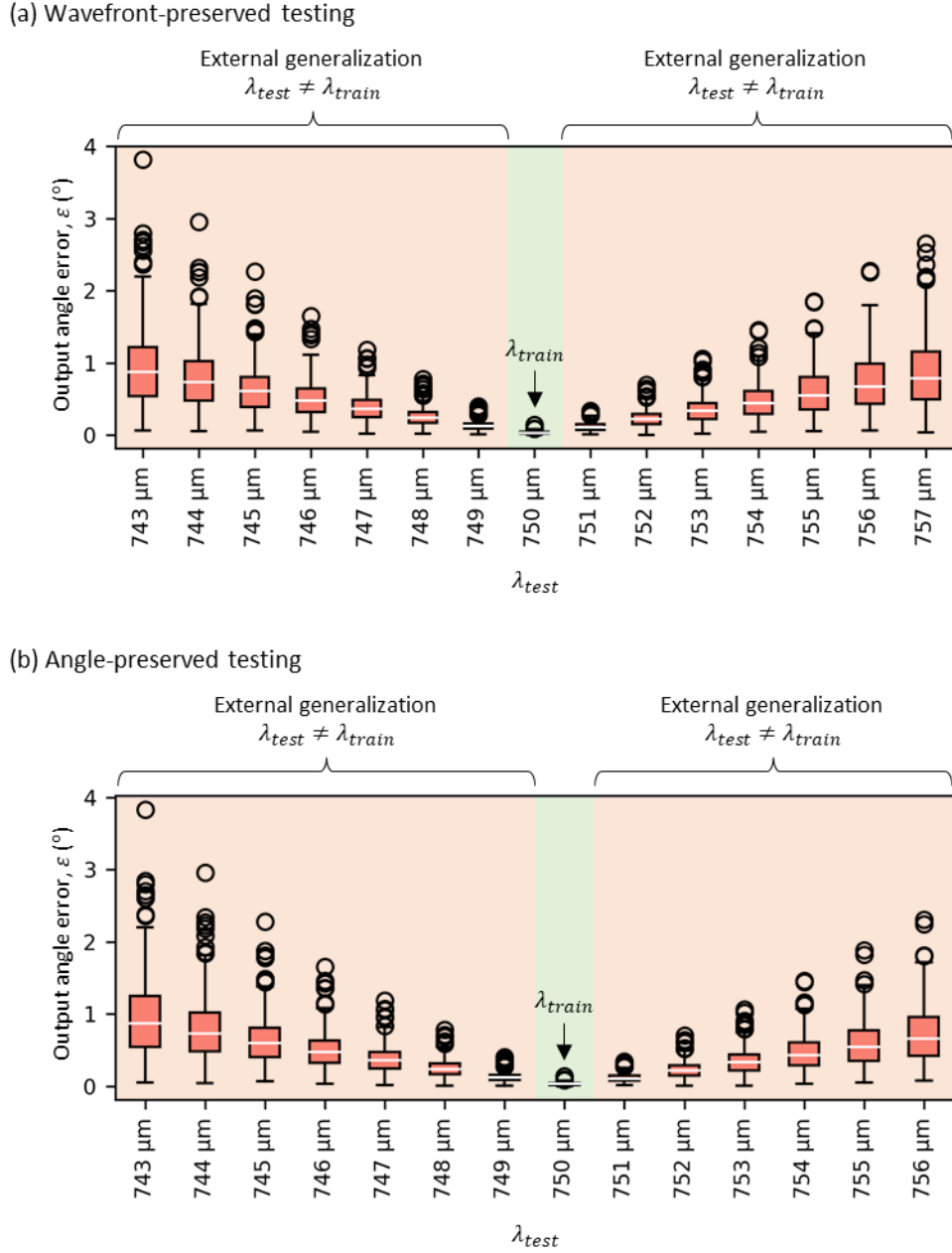


**Fig. 3:** Wavelength sensitivity of the performance of an RFG for an arbitrarily permuted refractive function. (a) Distribution of the output angle error as a function of the test wavelength  $\lambda_{test}$ , for the same RFG of Fig. 2, which was trained for an illumination wavelength of  $750 \mu\text{m}$ , i.e.,  $\lambda_{train} = 750 \mu\text{m}$ . For this plot in (a), the  $\theta$ -values associated with the input and target illumination directions are adjusted so that the corresponding wavefronts at the input and output apertures are identical to their training counterparts (referred to as wavefront-preserved testing). (b) For this plot, the  $\theta$ -values associated with the input and target directions are kept unchanged (referred to as angle-preserved testing). The distributions arise from the values corresponding to all the input directions.



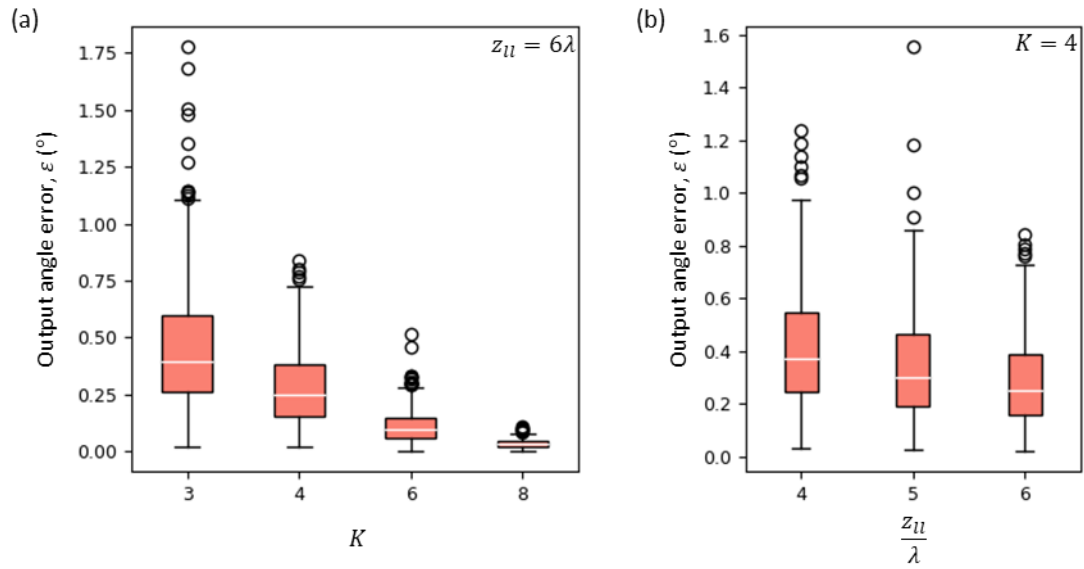


**Fig. 4:** The impact of  $K$  and  $z_{ll}$  on the performance of RFGs for an arbitrarily permuted refractive function. (a) Distribution of the output angle errors as a function of  $K$ , while  $z_{ll}$  is kept constant at  $\sim 6\lambda$ . Here the target refractive function is the one shown in Fig. 2a. (b) Distribution of the output angle errors as a function of  $z_{ll}$ , while  $K$  is kept constant at 4.



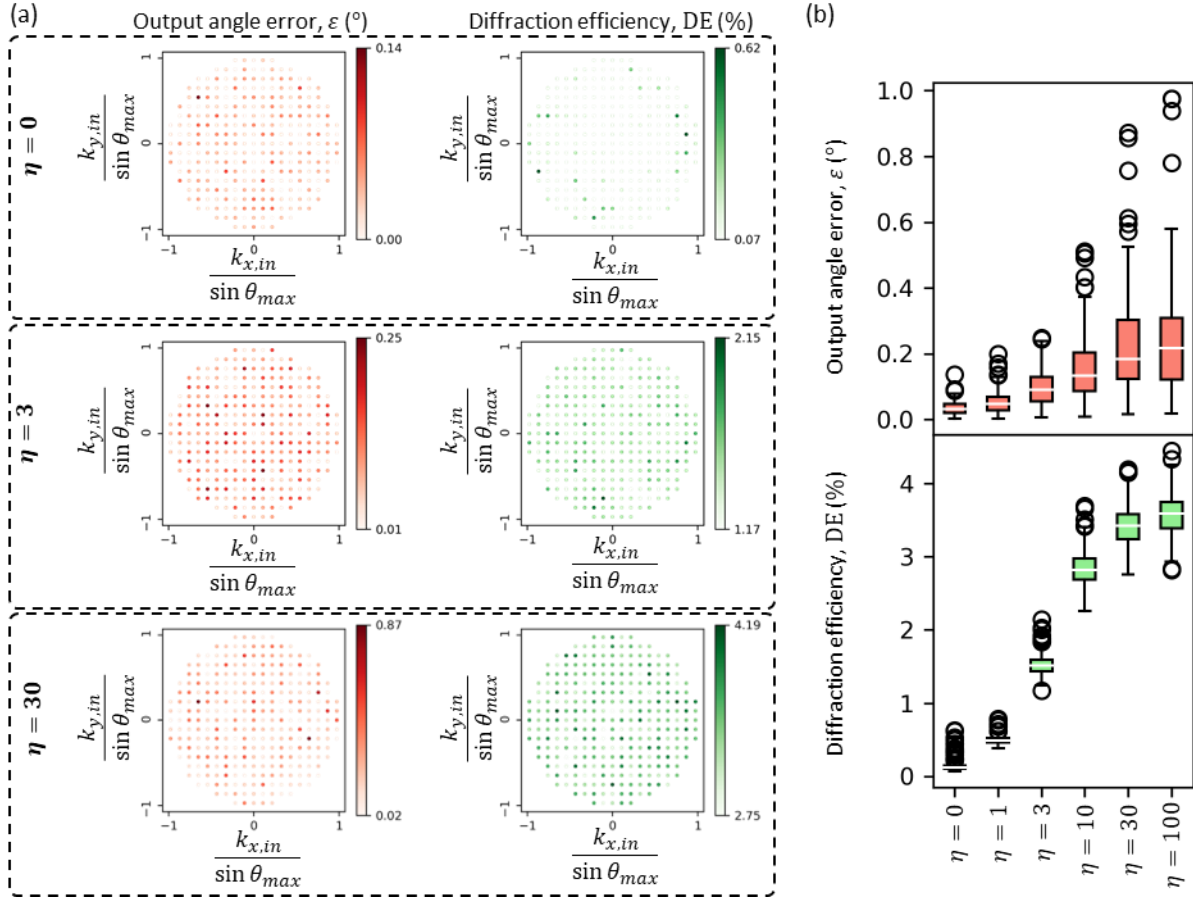


**Fig. 5:** Enhancement of the output diffraction efficiency of an RFG designed for an arbitrarily permuted refractive function. (a) Output angle errors and diffraction efficiencies of three different RFG designs trained with different values of the hyperparameter  $\eta$ . Here, the target refractive function is the one shown in Fig. 2a. (b) Distribution of output angle errors and diffraction efficiencies as a function of  $\eta$ . Each value of the training hyperparameter  $\eta$  corresponds to a separately optimized RFG design. For all the designs,  $K = 8$  and  $z_{ll} \approx 6\lambda$ .

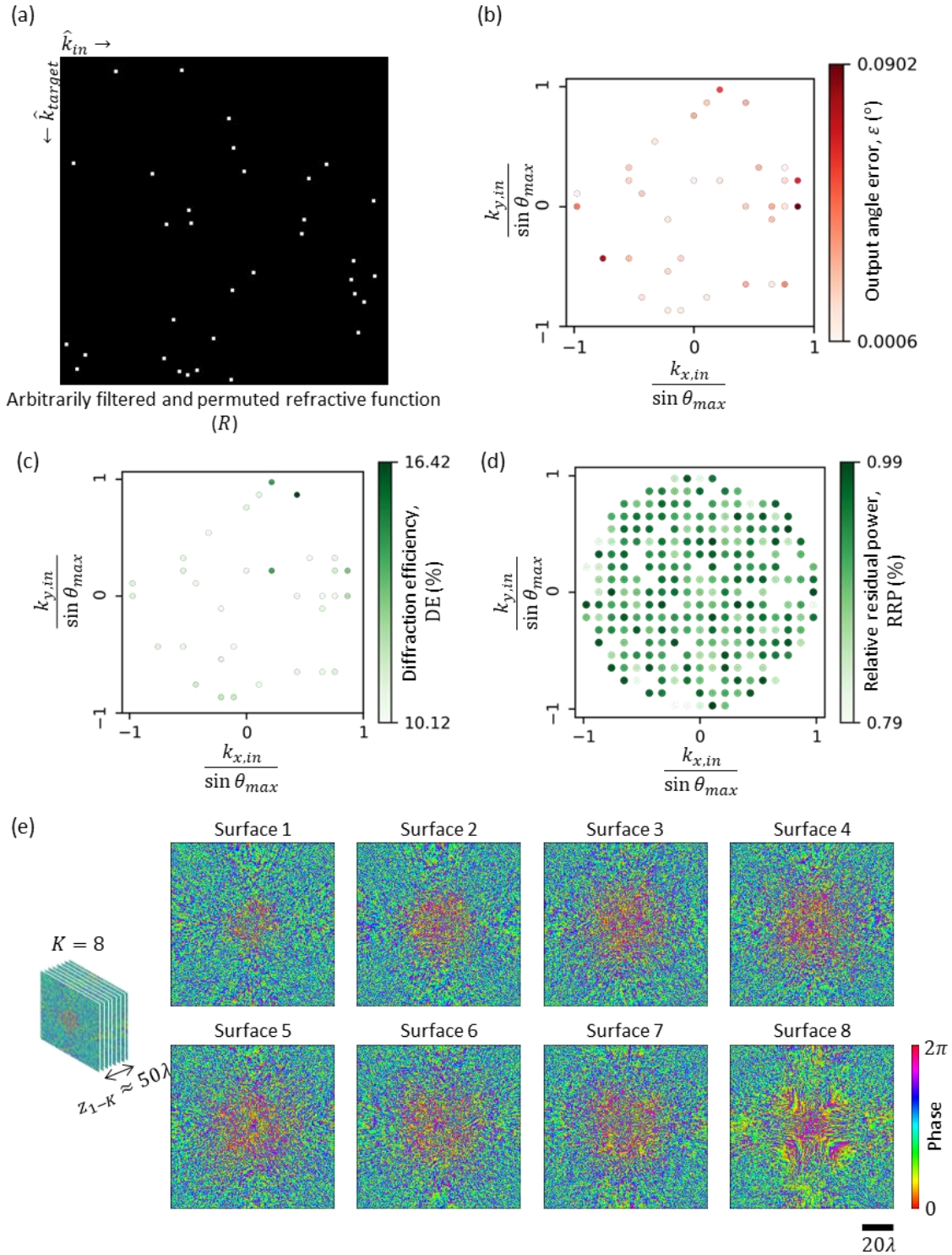


**Fig. 6:** Arbitrarily filtered and permuted refractive function implementation with a  $K = 8$  RFG design. (a) The matrix  $R$  representing an arbitrarily filtered and permuted refractive function. The ratio of the filtered directions is  $\sim 90\%$ . (b) Output angle error  $\varepsilon$  for all the unfiltered input directions. (c) Output diffraction efficiency  $DE$  for all the unfiltered input directions. (d) Relative residual power  $RRP$  for the filtered input directions. (e) The optimized phase profiles of the RFG surfaces.

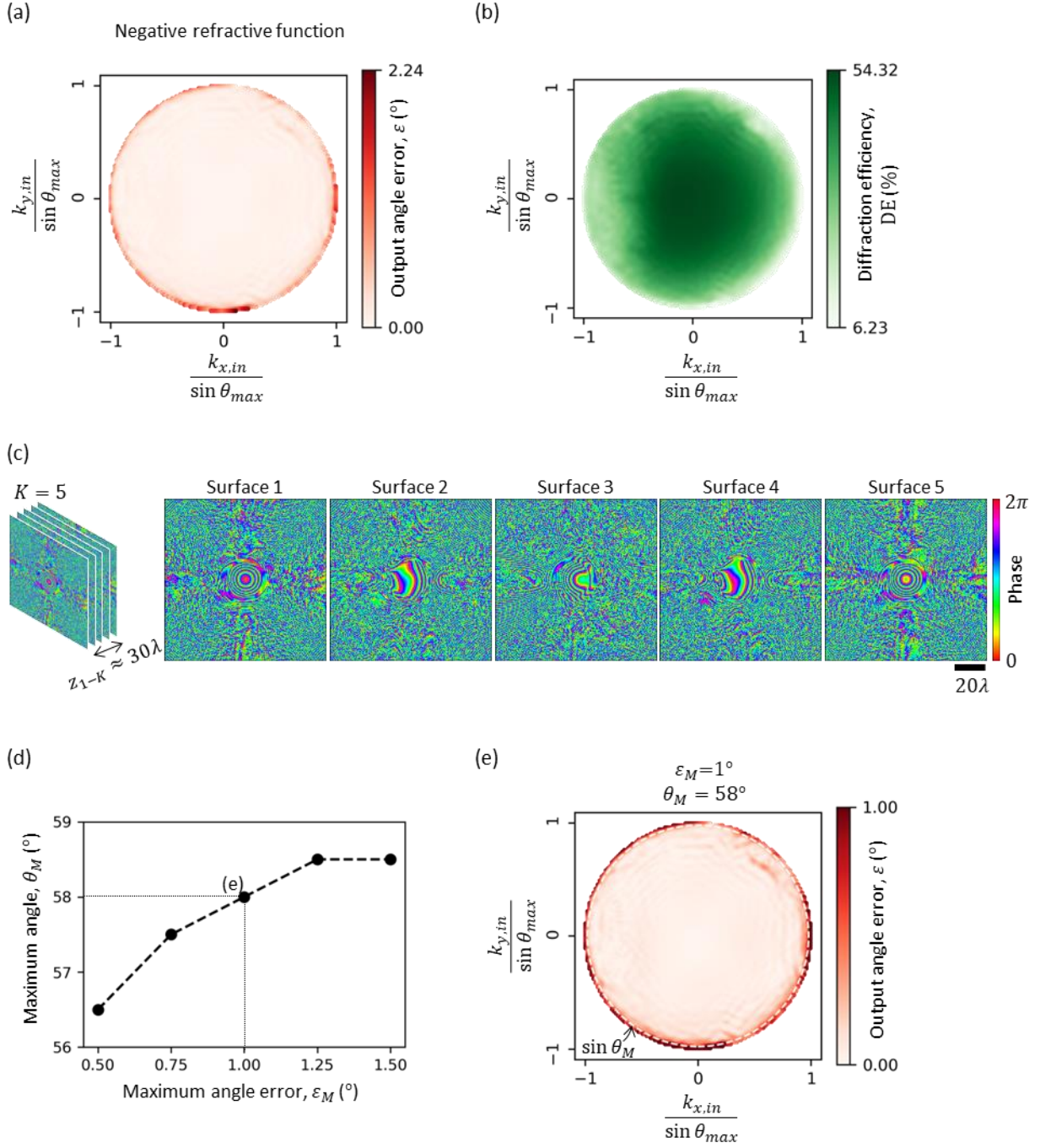


**Fig. 7:** Negative refractive function ( $\theta_{target} = \theta_{in}$ ,  $\varphi_{target} = \varphi_{in} + 180^\circ$  for all  $\theta_{in} < \theta_{max} = 60^\circ$ ) using a  $K = 5$  RFG design. (a) Output angle error for all the input directions, sampled densely. (b) Diffraction efficiency for all the input directions. (c) The optimized phase profiles of the RFG surfaces. The distance  $z_{ll}$  between consecutive surfaces is  $\sim 6\lambda$ , giving an axial distance of  $z_{1-K} \approx 30\lambda$  between the first and the last transmissive surfaces. (d) The operating curve of the RFG design, showing  $\theta_M$  (the maximum acceptable  $\theta_{in}$ ) as a function of the maximum acceptable angle error,  $\varepsilon_M$ . (e) When  $\varepsilon_M = 1^\circ$ ,  $\theta_M = 58^\circ$ , i.e., for all the input directions with  $\theta_{in} < 58^\circ$ , the output angle error is less than  $1^\circ$ .

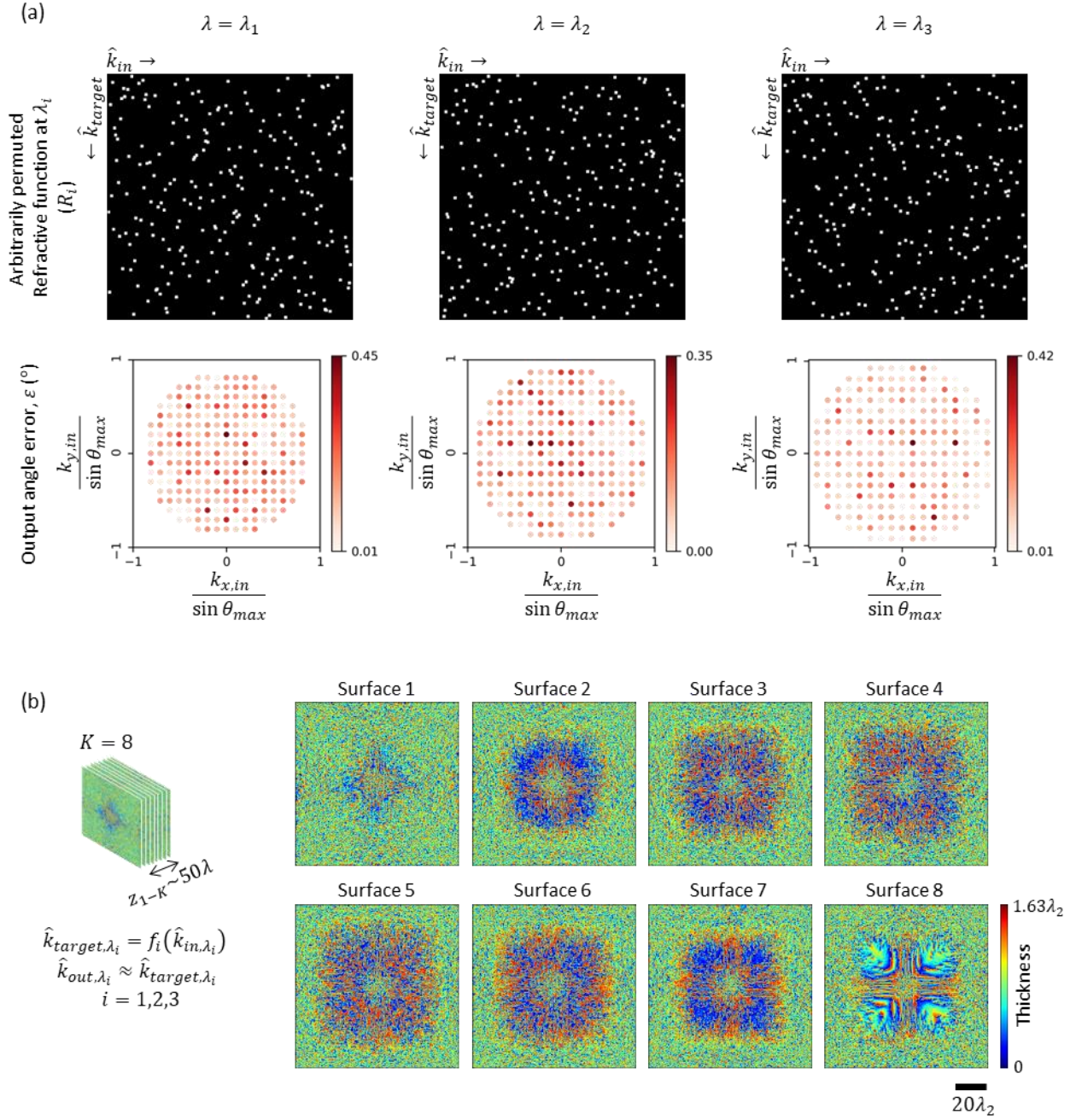


**Fig. 8:** Wavelength multiplexing of arbitrarily permuted refractive functions with an RFG. (a) The matrices representing the targeted arbitrarily permuted refractive functions at three distinct wavelengths (top row). The bottom row shows, for a  $K = 8$  RFG design, the error in the output angle as a function of the input direction at these three wavelengths. (b) The optimized thickness profiles of the RFG surfaces. The distance  $z_{ll}$  between consecutive surfaces is  $\sim 6\lambda$ , giving an axial distance of  $z_{1-K} \approx 50\lambda$  between the first and the last transmissive surfaces.



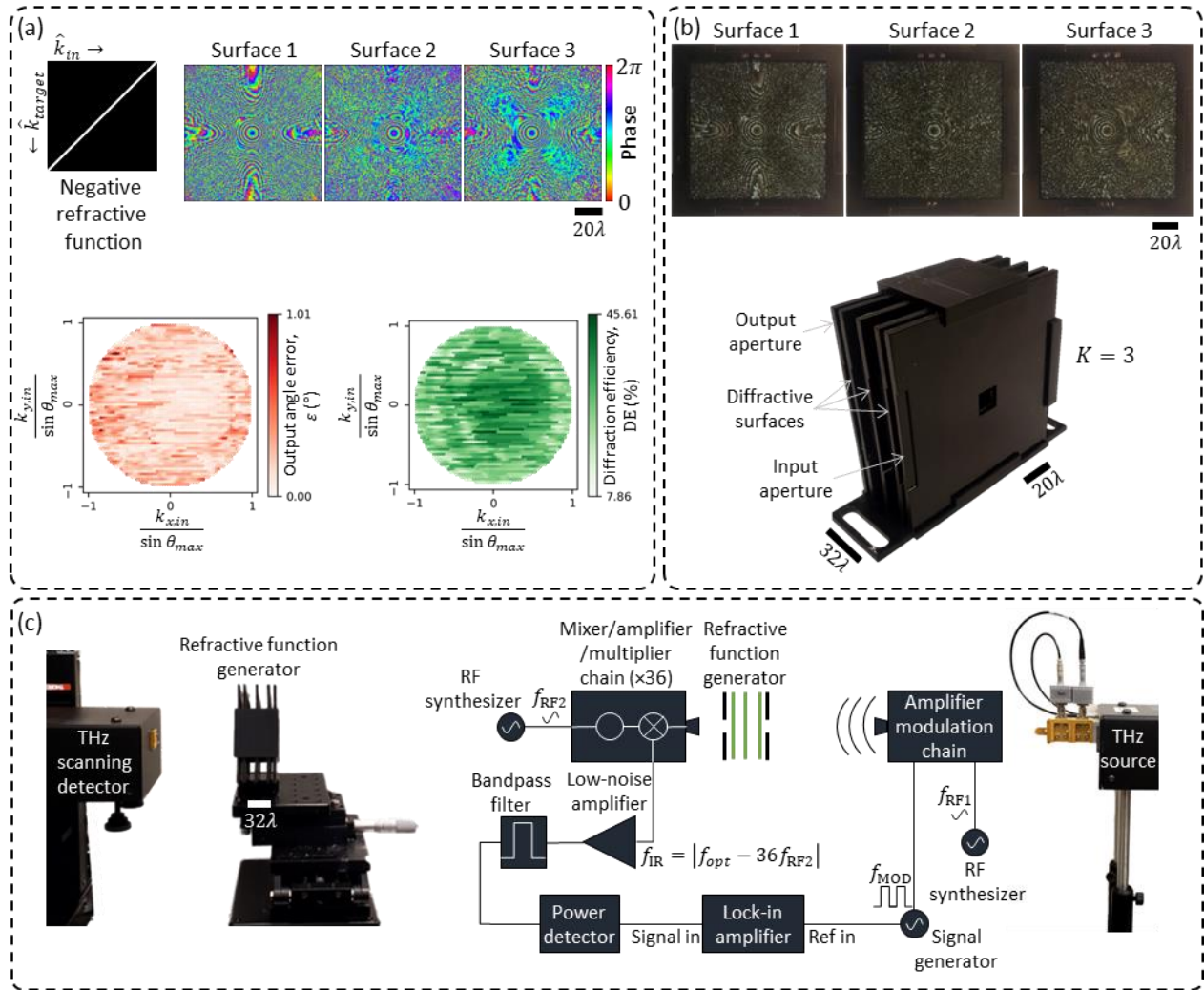


**Fig. 9:** Experimental demonstration of the negative refractive function at  $\lambda = 0.75$  mm. (a) The optimized phase profiles of a  $K = 3$  RFG for implementing negative refractive function with  $\theta_{max} = 30^\circ$ . Also shown are the output angle errors and the diffraction efficiencies obtained in simulation. (b) The RFG hardware, assembled from the structured surfaces and input/output apertures, fabricated using 3D-printing. (c) The THz setup comprising the source and the detector, together with the 3D-printed RFG.

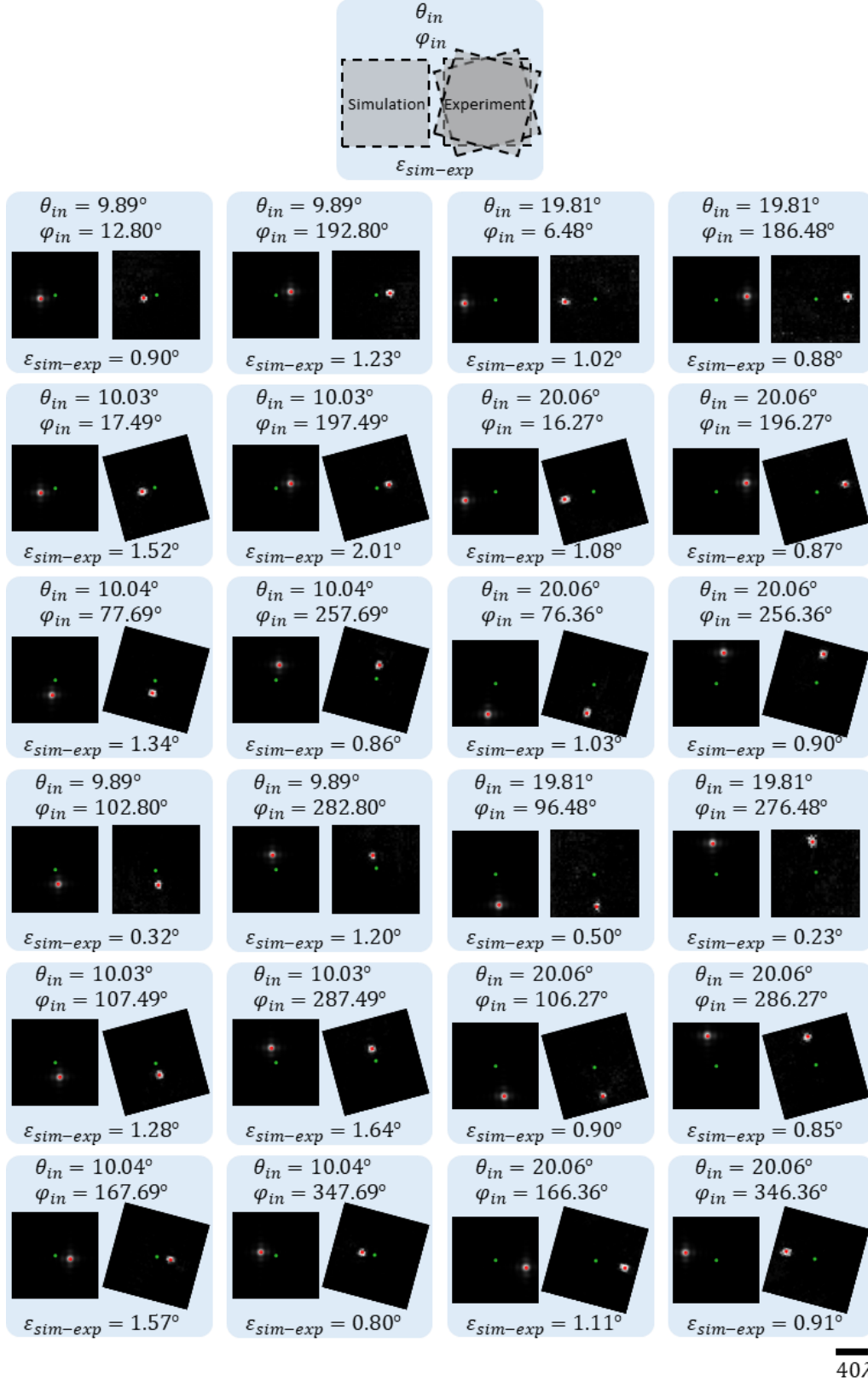


**Fig. 10:** Visualization and quantitative analysis of the experimental RFG results. Each panel corresponds to the input direction defined by  $(\theta_{in}, \varphi_{in})$  and compares the simulated and experimental diffraction

patterns measured at a distance of  $z = 80$  mm from the output aperture of the RFG (see Fig. 9c). The green dot marks the center (0,0) of the FOV and the red dot marks the first moment of the diffracted intensity pattern; also see Supplementary Fig. S1b. In each panel, the mismatch between the numerical simulation and the experimental result, defined as the angle  $\varepsilon_{sim-exp}$  between the simulated output wave and the experimentally measured output wave, is also reported.